Domain-Wall Topology Induced by Spontaneous Symmetry Breaking in Polariton Graphene

D.D. Solnyshkov, C. Leblanc, I. Septembre, G. Malpuech

Domain-wall topology induced by spontaneous symmetry breaking in polariton graphene

D. D. Solnyshkov,[1,2] C. Leblanc,[1] I. Septembre,[1] and G. Malpuech[1]

[1]*Institut Pascal, PHOTON-N2, Université Clermont Auvergne, CNRS, Clermont INP, F-63000 Clermont-Ferrand, France.*
[2]*Institut Universitaire de France (IUF), F-75231 Paris, France*

We present a numerical study of exciton-polariton (polariton) condensation in a staggered polariton graphene showing a gapped s-band. The condensation occurs at the kinetically-favorable negative mass extrema (K and K' valleys) of the valence band. Considering attractive polariton-polariton interaction allows to generate a spatially extended condensate. The symmetry breaking occurring during the condensate build-up leads to the formation of valley-polarized domains. This process can either be spontaneous, following the Kibble-Zurek scenario, or triggered, leading to a controlled spatial distribution of valley-polarized domains. The selection of a single valley breaks time-reversal symmetry, and the walls separating domains exhibit a reconfigurable topologically-protected chiral current. This current emerges as a result of the interplay between the non-trivial valley topology and the condensation-induced symmetry breaking.

Topological physics is now a well-developed field taught in the Universities. It has changed our understanding of physical systems and brought new approaches to their description. Topologically nontrivial crystals actually represent a significant fraction [1], and not a rare delicate case in solid state physics. Besides the fundamental change of the paradigm, topological physics also brings new applications ranging from topologically-protected qubits [2, 3] to topological lasers [4, 5] and optical isolators [6, 7].

In particular, staggered honeycomb lattices with two different atoms or sites in the unit cell are implemented naturally in boron nitrides [8], transitional metal dichalcogenides [9], but also in artificial optical lattices [10]. Honeycomb lattices show two Dirac valleys called K and K' at the corners of the Brillouin zone. The staggering opens a gap. Each valley can be approximately described by a 2D massive Dirac Hamiltonian. The corresponding states are characterized by Berry curvature, which can further be linked with a valley Chern number $\pm 1/2$ in both valleys respectively. The total Chern number including both valleys is zero and a staggered honeycomb lattice is topologically trivial as a whole, but it can still exhibit the quantum valley Hall effect [11, 12]. It consists in the formation of two states localized at the interface between regions with opposite staggering. Their propagation directions, determined by the difference between valley Chern numbers [10, 13, 14], depend on the valley.

In band properties calculations, the interactions between the particles are usually neglected. An important question that has no general answer is how the lattice topology combines with the many-body properties of a quantum fluid filling it [15]. For fermions, one generally studies the behavior of the Fermi surface, particularly such effects as Fermi arcs in Weyl semi-metals [16]. In the simplest approximation, the Fermi surface is obtained by filling the single-particle states with electrons, neglecting their interactions, justified by the Pauli exclusion principle [17]. Strongly interacting fermions in topological flat bands are promising for fractional quantum Hall effect [18–20]. Regarding bosons, the formation of a Bose-Einstein condensate in a lattice leads to spectacular topological effects [21]. A condensate can occupy a single-particle state, allowing to calculate the topology of its weak excitations (bogolons) [22–24] to probe the interactions-driven topological transitions [25–27]. Other situations include the formation of purely non-linear solutions (e.g. solitons) [28–30], often bifurcating from linear topological states [31–33]. In these cases, the topology of the lattice is inherited by the non-linear states [23, 31, 34].

Beyond the inheritance of the lattice properties, the quantum fluid can bring in its own topology, reinforcing the protection [35]. The topology of the bosonic quantum fluid is due to the phase of the wavefunction, whose winding number is a topological invariant [36]. It plays an important role in the Kibble-Zurek mechanism [37–39] (KZM), which consists in the formation of domains of the order parameter during second-order phase transitions, such as the Bose-Einstein condensation. These domains then decay into topologically-protected defects, whose density can be measured. The walls, separating these domains, can also behave as topological defects [40], lasting as long as the domains they surround.

In this work we show how the combination of lattice topology with the properties of an interacting bosonic quantum fluid leads to chiral currents in polariton condensates. We study polariton condensation in a uniform staggered honeycomb lattice (without quantum valley Hall interface). Condensation is kinetically favored in the negative mass K and K' states at the top of the valence band. We consider attractive polariton-polariton interactions allowing a spatially homogeneous condensate. Spontaneous symmetry breaking by phase fluctuations creates valley-polarized spatial domains for the con-

densate wavefunction. The domain size is correctly described by a mean-field Kibble-Zurek scaling exponent. The domain walls, appearing as stable topological defects, separate valley-polarized domains characterized by opposite valley Chern numbers. We also show that one can locally trigger condensation in a given valley, thus controlling the spatial distribution of valley-polarized domains. Because of the valley polarization, the reconfigurable domain walls sustain a *single* unidirectional mode, contrary to the quantum valley Hall interfaces. The nonlinear wavefunction of the domain wall and the corresponding topological one-way currents are analytically described by a solution similar to a Jackiw-Rebbi [41] soliton. At longer times, the system evolves towards a single valley-polarized domain.

We consider a patterned microcavity under non-resonant pumping. The pattern forms a staggered honeycomb lattice with different energies on the A and B sites and a trivial gap at the Dirac point. The patterning of honeycomb and other lattices is now well-established [42–45]. The Dirac cones have been observed in polariton graphene [42, 46], and the topological edge states were evidenced experimentally [47]. Condensation has already been observed in polariton graphene at various points of the dispersion [42, 47, 48]. In particular, condensation at the Dirac point, with a gap opened by an applied magnetic field, was observed in Ref. [47]. This is also supported by recent theoretical studies [49].

We simulate polariton relaxation and condensation under non-resonant pumping using the Gross-Pitaevskii equation with lifetime, energy relaxation, and saturated gain [42, 50]:

$$\begin{aligned} i\hbar\frac{\partial\psi}{\partial t} &= -(1-i\Lambda)\,\frac{\hbar^2}{2m}\Delta\psi + g\,|\psi|^2\,\psi \\ &+ \left(U_0 + U_R + i\gamma(|\psi|^2) - i\Gamma\right)\psi + \chi \end{aligned} \qquad (1)$$

Here, m is the polariton mass, g is the polariton-polariton interaction constant, U_0 is the potential forming the staggered honeycomb lattice of polariton graphene with different site radii, U_R is the repulsive potential of the reservoir. $\gamma(|\psi|^2)$ is the saturated gain term [51]. Γ is the polariton decay time, χ is the noise describing the spontaneous scattering from the excitonic reservoir, and Λ characterizes the efficiency of the energy relaxation [52]. We solve Eq. 1 numerically, choosing the parameters of a typical polariton graphene lattice [42, 53]. This equation was successfully used to describe polariton condensation at the Γ point at the top of the s-band [42] (negative mass states) and to study the KZM at the bottom of the band [54]. The state where the condensate forms depends on the condensation parameters such as the lifetime of the states and on the energy relaxation efficiency [55–57]. The latter can be controlled via the detuning (determining the excitonic fraction) and via the spot size [58, 59].

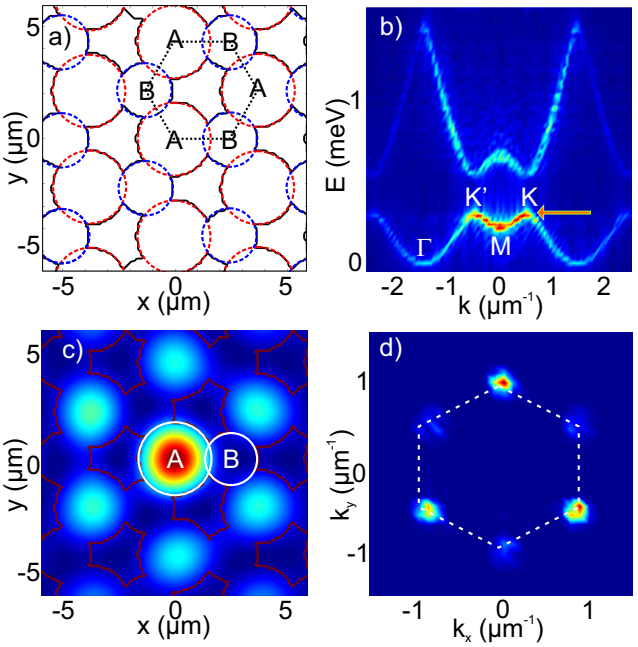

FIG. 1: (a) Contour plot of the lattice potential showing a honeycomb unit cell (black dots) with sites A (magenta circles) and B (blue circles). (b) Dispersion of the polariton graphene showing a gap at the K point. (c) Spatial distribution of intensity corresponding to a single valley K. d) Condensed state in the reciprocal space exhibiting high intensity at the K points of the Brillouin zone.

We begin by examining the properties of the linear states of the lattice. We take $\Lambda = g = \gamma = 0$ in (1). We consider a narrow Gaussian wavepacket as an initial condition and Fourier-transform the solution $\psi(\boldsymbol{r}, t)$ to obtain the dispersion $|\psi(\boldsymbol{k}, E)|^2$. Fig. 1(a) shows the real space image of the confinement potential (black lines) with the sites A and B (magenta and blue) forming the unit cell (black dots). Fig. 1(b) shows a cut of the dispersion centered at the M point, with a gap at the K points. Its size is controlled by the difference of the radius of the sites A and B. Panel (c), similar to panel (a), shows the particle density $|\psi_K(x, y)|^2$ of the eigenstate at the K point at the top of the lowest energy band. The two sites A and B are marked with white lines. For the valley extrema at the top of the valence band, $|\psi_A|^2 \gg |\psi_B|^2$ because of the staggering. The specific microcavity platform [60] allows a full experimental access (both in detection and excitation) to eigenstates both in real and reciprocal space through angular, spatially, energy- and time-resolved spectroscopy [42, 61].

We now study the polariton relaxation and condensation in this lattice. To simulate condensation, we consider a stationary spatially homogeneous pumping and exciton distribution providing the gain γ_r. We then solve Eq. (1) versus time. We consider attractive polariton-polariton interactions ($g < 0$). Because of the negative

mass $m_{eff} < 0$, these attractive interactions become effectively repulsive. An attractive polariton-polariton interaction can show up as a result of the interplay between the reservoir and condensate dynamics [62] or from the polariton Feshbach resonance [63, 64] related to the biexcitons, which can be accessed by changing the exciton-photon detuning. (See [65] for the more usual case of repulsive interactions.) For a particular set of parameters [53], it is possible to obtain condensation at the Dirac points, as confirmed by the momentum space distribution of the condensate immediately after its formation ($t \approx t_c$) shown in Fig. 1(d).

This is explained by the decay rates (Fig. 2(a)), averaging the linear eigenstates over k at each energy. The radiative decay in Eq. (1) reads $\Gamma = \Gamma_0 + \Gamma_E$ where Γ_0 related to the losses through the cavity mirrors is energy-independent. Γ_E (black points), proportional to the intensity of the field at the surfaces of the pillars, is energy-dependent. The related losses are due to disorder [42, 66] and to the suppression of radiative emission by destructive interference [67]. The anti-symmetric states at the top of bands have a smaller decay via these surface losses. The other sources of decay are scattering thermalization processes, taken into account by the Λ coefficient in Eq. (1), which scale linearly with the energy of the states [52, 54] (red points). The sum of both rates is plotted in green: it exhibits a minimum at the top of the first band, favoring condensation at the degenerate K and K' points.

Condensation occurs in the K and K' states at the top of the valence band, because these states show the longest lifetime (see Fig. 2(a)). Phase fluctuations present during the dynamical condensation process provoke local symmetry breaking. This leads to the formation of valley-polarized domains separated by domain walls (Fig. 2(b)) at $t = t_c$. At longer times $t > t_c$, the valley-polarized domains change size, to finally form a single valley-polarized domain. The valley selectivity is driven by the net gain efficiency: a single valley provides a higher gain and smaller losses than a superposition of valleys [65].

This dynamics can be studied in single-shot experiments. Moreover, using a Hanbury Brown–Twiss configuration [65], it is possible to measure valley correlation degree $V(r - r', t)$ as a function of time in periodic pulsed experiments with a long pulse duration [56]. The simulated $V(r - r', t)$, averaged over 20 periods and over 250×250 detection regions $\boldsymbol{r}$ and $\boldsymbol{r'}$ is shown in Fig. 2(c). At $t = t_c$, valley correlation drops to 0.5 (no correlation) at the scale of 30 μm, while at $t = t_c + 1.5$ ns only a slight decrease is seen at 50 μm. This increase of the valley coherence indicates the growth of the average domain size, accompanied by the decrease of their number. Figure 2(d) shows the time evolution of the mean condensate density and of the number of domains. The final valley polarization achieved (K or K') is randomly chosen for each experiment. This long-time result is similar

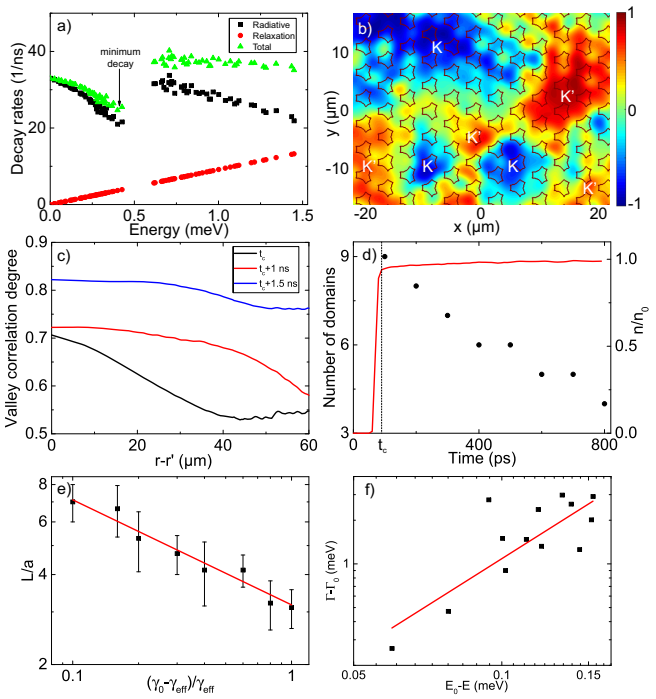

FIG. 2: a) Decay rates in polariton graphene (black - radiative, red - relaxation, green - total); b) Valley-polarized domains in real space; c) Valley correlation degree for $t = t_c, t_c + 1$ ns, $t_c + 1.5$ ns (black, red, blue); d) Number of domains and total particle density as functions of time; e) The domain size scaling with quench parameter (black dots with error bars) with a power law fit (red line); f) Scaling of the decay rate at the band edge (black dots) with a power law fit (red line).

Ref. [49].

The formation of domains in second-order phase transitions is described by the Kibble-Zurek mechanism, where the quench time is controlled by the normalized pumping density $\tau_Q^{-1} \sim (\gamma_0 - \gamma_{eff})/\gamma_{eff}$, where γ_0 is the reservoir gain controlled by the pumping and γ_{eff} is its critical value, below which the condensation does not occur [54, 68]. The dependence of the size of valley-polarized domains versus the quenching parameter [39] is shown in Fig. 2(e). It follows a power law decay with a scaling exponent $\eta = -0.34 \pm 0.03$. Each point is averaged over 7 simulations, with error bars representing the standard deviation. In the mean-field approximation the KZM scaling exponent for the domain size reads:

$$\eta = -(D - d)\frac{\nu}{1 + z\nu} \qquad (2)$$

where $D = 2$ and $d = 1$ are the space and domain wall dimensionalities. $z\nu$ is the dynamical scaling exponent, given by the energy dependence of the total decay rate at the band edge (Fig. 2(a)). Figure 2(f) shows the decay rate as a function of energy [69]. Its scaling is 2.1 ± 0.3, consistent with a dynamical scaling exponent $z\nu = 2$.

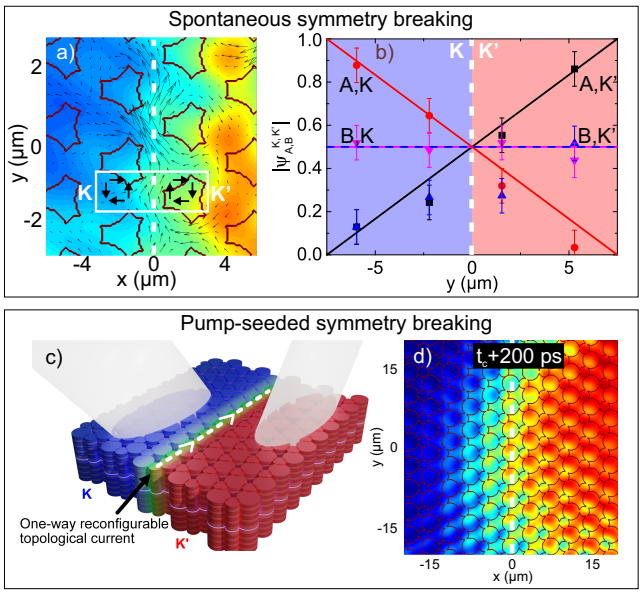

FIG. 3: (a) Two valley-polarized domains (false color shows the valley polarization) with a boundary (white dashed line) exhibiting a localized one-way current (black arrows). The effective fields of the two occupied valleys with opposite windings are shown with black arrows in the white rectangle. (b) The wavefunction components across the interface: numerics (dots) and analytical ansatz (lines); (c) Seeded condensation scheme; (d) Seeded domain stability.

Together with the critical exponent $\nu = 1$ appearing due to the linear dispersion of the Dirac cone [54], this gives a mean-field KZM scaling exponent $\eta = -1/3$, in excellent agreement with numerical simulations (Fig. 2(e)).

We now study the domain walls, where the continuity of the condensate wavefunction needs to be ensured. Figure 3(a) shows the quantum-mechanical current (arrows) together with valley polarization (false color), plotted for a particular realization of the condensate. No net current is flowing through the sites within the domains, while the domain wall (white dashed line) clearly carries a net upward current.

This one-way interface current with deep topological roots is qualitatively similar to the well-known chiral Jackiw-Rebbi [41, 70] interface state. In the classical Jackiw-Rebbi case, the topology of each region is determined by the mass sign, and its change guarantees the existence of the interface state. In our case, the Hamiltonian on both sides of the domain wall is the same (and describes both valleys), it is the wavefunction, which is the solution of the non-linear Dirac equation, which changes its valley polarization across the domain wall. The domains and the domain walls are therefore dynamical objects capable of evolution. However, the origin of chirality is the same in both cases, as shown below.

The spatial image in Fig. 3(a) shows the interface and the distribution of the effective field in the two valleys with opposite windings (the arrows inside the white rectangle). This system can be described with a 4×4 block-diagonal Hamiltonian composed of two 2D Dirac Hamiltonians with opposite winding. Including the on-site interactions (valley-isotropic, but site-dependent), the explicit stationary non-linear Dirac equation reads:

$$\begin{pmatrix} \Delta + g\left|\psi_A^K\right|^2 + g\left|\psi_A^{K'}\right|^2 & \hbar c\left(-\frac{\partial}{\partial x} - i\frac{\partial}{\partial y}\right) & 0 & 0 \\ \hbar c\left(+\frac{\partial}{\partial x} - i\frac{\partial}{\partial y}\right) & -\Delta + g\left|\psi_B^K\right|^2 + g\left|\psi_B^{K'}\right|^2 & 0 & 0 \\ 0 & 0 & \Delta + g\left|\psi_A^K\right|^2 + g\left|\psi_A^{K'}\right|^2 & \hbar c\left(+\frac{\partial}{\partial x} - i\frac{\partial}{\partial y}\right) \\ 0 & 0 & \hbar c\left(-\frac{\partial}{\partial x} - i\frac{\partial}{\partial y}\right) & -\Delta + g\left|\psi_B^K\right|^2 + g\left|\psi_B^{K'}\right|^2 \end{pmatrix} \begin{pmatrix} \psi_A^K \\ \psi_B^K \\ \psi_A^{K'} \\ \psi_B^{K'} \end{pmatrix} = E \begin{pmatrix} \psi_A^K \\ \psi_B^K \\ \psi_A^{K'} \\ \psi_B^{K'} \end{pmatrix} \tag{3}$$

where Δ is the mass term due to the graphene staggering, identical for both valleys, and g is the on-site interaction constant. Far from the interface, the valley-polarized condensate wavefunctions are given by $\psi_{+\infty} = (1,0,0,0)^T$ and $\psi_{-\infty} = (0,0,1,0)^T$. These boundary conditions are induced by the spontaneous symmetry breaking during the condensation. Exactly at the interface, all 4 components have to be non-zero in order to satisfy Eq. (3).

We find that the solution of the non-linear Dirac equation (3) with two valley-polarized regions and a domain wall between them can be written as $|\psi\rangle \approx (1/2 + ax, 1/2, 1/2 - ax, 1/2)^T \exp(ik_y y)$. This solution is valid to the first order in x and k_y near $x = 0$ (see [65] for details), with $a = \Delta/\hbar c$ (the inverse Compton wavelength, recently associated with the quantum metric [71]) and $E = \Delta + g/2 + \hbar c k_y$ (with $\Delta < 0$ and $g < 0$). It is shown in Fig. 3(b) with lines (color corresponds to the wavefunction components), together with the points, extracted from the wavefunction of the numerical experiment shown in Fig. 3(a). Their good agreement confirms the validity of the analytics.

From $E(k_y)$, we obtain the group velocity $+c$ along the y axis. Its well-defined sign indicates a one-way state.

The opposite direction is forbidden [65]. The opposite behavior of ψ_A^K and $\psi_A^{K'}$ across the domain wall is possible thanks to the opposite valleys winding ($\pm\partial/\partial x$ in (3)). The constant sign of $\partial/\partial y$ provides a single direction for the current along the interface. We thus conclude that the chiral localized current along the domain wall solution of the non-linear Dirac equation has the same origin as the chiral interface state in linear Dirac equation with inverted mass (Jackiw-Rebbi): the opposite topology on both sides of the interface. Its localization length is determined by the gap size $l = 1/a = \hbar c/\Delta$.

These valley-polarized domains can be created in a controlled way, by seeding the condensation with probes specifically exciting K and K' points in adjacent regions, as shown in Fig. 3(c). The resulting regions are stable over hundreds of picoseconds, as confirmed by Fig. 3(d), showing the valley polarization degree at $t_c + 200$ ps. This is long enough to allow one-way information transfer along the interface (thanks to the high group velocity), after which the system can be reconfigured [65]. Interestingly, valley condensation can be observed even in non-patterned cavities [72].

To conclude, we have shown that condensation can occur at the Dirac points in staggered polariton graphene. Under homogeneous pumping with repulsive effective interactions, valley-polarized domains form via the Kibble-Zurek mechanism. Stable domain walls between such domains are carrying topological one-way currents. They can be created in a controlled way for applied purposes.

We acknowledge the support of the European Union's Horizon 2020 program, through a FET Open research and innovation action under the grant agreement No. 964770 (TopoLight), project ANR Labex GaNEXT (ANR-11-LABX-0014), and of the ANR program "Investissements d'Avenir" through the IDEX-ISITE initiative 16-IDEX-0001 (CAP 20-25).

[1] M. G. Vergniory, L. Elcoro, C. Felser, N. Regnault, B. A. Bernevig, and Z. Wang, Nature **566**, 480 (2019).
[2] S. Das Sarma, M. Freedman, and C. Nayak, Phys. Rev. Lett. **94**, 166802 (2005).
[3] S. Gladchenko, D. Olaya, E. Dupont-Ferrier, B. Doucot, L. B. Ioffe, and M. E. Gershenson, Nat. Phys. **5**, 48 (2009).
[4] B. Bahari, A. Ndao, F. Vallini, A. El Amili, Y. Fainman, and B. Kanté, Science (New York, N.Y.) **358**, 636 (2017).
[5] M. A. Bandres, S. Wittek, G. Harari, M. Parto, J. Ren, M. Segev, D. N. Christodoulides, and M. Khajavikhan, Science (New York, N.Y.) **359**, aar4005 (2018).
[6] D. D. Solnyshkov, O. Bleu, and G. Malpuech, Applied Physics Letters **112**, 31106 (2018), ISSN 0003-6951.
[7] D. Karki, R. El-Ganainy, and M. Levy, Phys. Rev. Applied **11**, 034045 (2019).
[8] K. S. Novoselov, D. Jiang, F. Schedin, T. Booth, V. Khotkevich, S. Morozov, and A. K. Geim, Proceedings of the National Academy of Sciences **102**, 10451 (2005).
[9] K. Novoselov, o. A. Mishchenko, o. A. Carvalho, and A. C. Neto, Science **353** (2016).
[10] J. Noh, S. Huang, K. P. Chen, and M. C. Rechtsman, Phys. Rev. Lett. **120**, 063902 (2018).
[11] D. Xiao, W. Yao, and Q. Niu, Phys. Rev. Lett. **99**, 236809 (2007).
[12] W. Yao, S. A. Yang, and Q. Niu, Phys. Rev. Lett. **102**, 096801 (2009).
[13] T. Ma, A. B. Khanikaev, S. H. Mousavi, and G. Shvets, Phys. Rev. Lett. **114**, 127401 (2015).
[14] L. Ju, Z. Shi, N. Nair, Y. Lv, C. Jin, J. Velasco, C. Ojeda-Aristizabal, H. A. Bechtel, M. C. Martin, A. Zettl, et al., Nature **520**, 650 (2015).
[15] E. J. Bergholtz and Z. Liu, International Journal of Modern Physics B **27**, 1330017 (2013).
[16] S.-Y. Xu, I. Belopolski, N. Alidoust, M. Neupane, G. Bian, C. Zhang, R. Sankar, G. Chang, Z. Yuan, C.-C. Lee, et al., Science **349**, 613 (2015).
[17] N. W. Ashcroft and N. D. Mermin, Solid State Physics (Harcourt, Inc. (New York, USA), 1976).
[18] E. Tang, J.-W. Mei, and X.-G. Wen, Phys. Rev. Lett. **106**, 236802 (2011), URL https://link.aps.org/doi/10.1103/PhysRevLett.106.236802.
[19] T. Neupert, L. Santos, C. Chamon, and C. Mudry, Phys. Rev. Lett. **106**, 236804 (2011), URL https://link.aps.org/doi/10.1103/PhysRevLett.106.236804.
[20] K. Sun, Z. Gu, H. Katsura, and S. Das Sarma, Phys. Rev. Lett. **106**, 236803 (2011), URL https://link.aps.org/doi/10.1103/PhysRevLett.106.236803.
[21] Z. Wu, L. Zhang, W. Sun, X.-T. Xu, B.-Z. Wang, S.-C. Ji, Y. Deng, S. Chen, X.-J. Liu, and J.-W. Pan, Science **354**, 83 (2016).
[22] G. Engelhardt and T. Brandes, Phys. Rev. A **91**, 053621 (2015).
[23] S. Furukawa and M. Ueda, New Journal of Physics **17**, 115014 (2015).
[24] M. Aidelsburger, M. Lohse, C. Schweizer, M. Atala, J. T. Barreiro, S. Nascimbène, N. Cooper, I. Bloch, and N. Goldman, Nature Physics **11**, 162 (2015).
[25] O. Bleu, D. D. Solnyshkov, and G. Malpuech, Phys. Rev. B **93**, 085438 (2016), URL https://link.aps.org/doi/10.1103/PhysRevB.93.085438.
[26] Y. Hadad, J. C. Soric, A. B. Khanikaev, and A. Alù, Nature Electronics **1**, 178 (2018), ISSN 2520-1131.
[27] L. J. Maczewsky, M. Heinrich, M. Kremer, S. K. Ivanov, M. Ehrhardt, F. Martinez, Y. V. Kartashov, V. V. Konotop, L. Torner, D. Bauer, et al., Science **370**, 701 (2020).
[28] Y. Lumer, Y. Plotnik, M. C. Rechtsman, and M. Segev, Phys. Rev. Lett. **111**, 243905 (2013).
[29] D. D. Solnyshkov, O. Bleu, B. Teklu, and G. Malpuech, Physical Review Letters **118**, 023901 (2017), ISSN 10797114, 1607.01805.
[30] D. Smirnova, D. Leykam, Y. Chong, and Y. Kivshar, Applied Physics Reviews **7**, 021306 (2020), https://doi.org/10.1063/1.5142397.
[31] M. S. Kirsch, Y. Zhang, M. Kremer, L. J. Maczewsky, S. K. Ivanov, Y. V. Kartashov, L. Torner, D. Bauer, A. Szameit, and M. Heinrich, Nat. Phys. **17**, 995 (2021).
[32] S. Mukherjee and M. C. Rechtsman, Science **368**, 856 (2020).
[33] M. Guo, S. Xia, N. Wang, D. Song, Z. Chen, and J. Yang, Opt. Lett. **45**, 6466 (2020).
[34] N. Pernet, P. St-Jean, D. D. Solnyshkov, G. Malpuech,

N. Carlon Zambon, Q. Fontaine, B. Real, O. Jamadi, A. Lemaître, M. Morassi, et al., Nature Physics pp. 1–7 (2022).
[35] O. Bleu, G. Malpuech, and D. D. Solnyshkov, Nature Comm **9**, 3991 (2018).
[36] D. J. Thouless, Topological Quantum Numbers in Nonrelativistic Physics (World Scientific Publishing Co, Singapore, 1998).
[37] T. Kibble, J. Phys. A.:Math. Gen. **9**, 1387 (1976).
[38] W. Zurek, Nature **317**, 505 (1985).
[39] W. Zurek, Physics Reports **276**, 177 (1996).
[40] K.-X. Yao, Z. Zhang, and C. Chin, Nature **602**, 68 (2022).
[41] R. Jackiw and C. Rebbi, Phys. Rev. D **13**, 3398 (1976).
[42] T. Jacqmin, I. Carusotto, I. Sagnes, M. Abbarchi, D. D. Solnyshkov, G. Malpuech, E. Galopin, A. Lemaître, J. Bloch, and A. Amo, Phys. Rev. Lett. **112**, 116402 (2014).
[43] S. Klembt, T. H. Harder, O. A. Egorov, K. Winkler, H. Suchomel, J. Beierlein, M. Emmerling, C. Schneider, and S. Höfling, Applied Physics Letters **111**, 231102 (2017).
[44] C. E. Whittaker, E. Cancellieri, P. M. Walker, D. R. Gulevich, H. Schomerus, D. Vaitiekus, B. Royall, D. M. Whittaker, E. Clarke, I. V. Iorsh, et al., Phys. Rev. Lett. **120**, 097401 (2018).
[45] B. Real, O. Jamadi, M. Milićević, N. Pernet, P. St-Jean, T. Ozawa, G. Montambaux, I. Sagnes, A. Lemaître, L. Le Gratiet, et al., Phys. Rev. Lett. **125**, 186601 (2020).
[46] M. Milićević, G. Montambaux, T. Ozawa, O. Jamadi, B. Real, I. Sagnes, A. Lemaître, L. Le Gratiet, A. Harouri, J. Bloch, et al., Phys. Rev. X **9**, 031010 (2019).
[47] S. Klembt, T. Harder, O. Egorov, K. Winkler, R. Ge, M. Bandres, M. Emmerling, L. Worschech, T. Liew, M. Segev, et al., Nature **562**, 552 (2018).
[48] H. Suchomel, S. Klembt, T. H. Harder, M. Klaas, O. A. Egorov, K. Winkler, M. Emmerling, R. Thomale, S. Höfling, and C. Schneider, Physical Review Letters **121**, 257402 (2018).
[49] C. Lledo, I. Carusotto, and M. H. Szymanska, scipost:202104.00031 (2021).
[50] E. Wertz, A. Amo, D. D. Solnyshkov, L. Ferrier, T. C. H. Liew, D. Sanvitto, P. Senellart, I. Sagnes, A. Lemaître, A. V. Kavokin, et al., Phys. Rev. Lett. **109**, 216404 (2012), URL `https://link.aps.org/doi/10.1103/PhysRevLett.109.216404`.
[51] The saturated gain is given by $\gamma(|\psi|^2) = \gamma_0(n_R)\exp(-n_{tot}/n_s)$ with $n_{tot} = \int |\psi|^2\, dxdy$ the total particle density, n_s the saturation density, and n_R the exciton reservoir density.
[52] P. LP, Sov. Phys. JETP **35**, 282 (1959).
[53] The parameters used in numerical simulations are: the polariton mass $m = 3 \times 10^{-5} m_0$ (m_0 is the free electron mass), the constant radiative decay $\Gamma_0 = \hbar/30$ ps, energy relaxation efficiency $\Lambda = 6 \times 10^{-3}$, interaction constant $\alpha = \pm 2\ \mu\text{eV}\cdot\mu\text{m}^2$, saturation density $n_s = 10^3\ \mu\text{m}^{-2}$, honeycomb lattice parameter 2.5 μm, pillar radius $r_A = 1.65\ \mu$m, $r_B = 1.2\ \mu$m, effective barrier height 20 meV. The simulations are carried out using the 3rd-order Adams method for the time derivative and a GPU-accelerated FFT for the Laplacian.
[54] D. D. Solnyshkov, L. Bessonart, A. Nalitov, and G. Malpuech, Phys. Rev. B **104**, 035423 (2021).
[55] J. Kasprzak, D. D. Solnyshkov, R. André, L. S. Dang, and G. Malpuech, Phys. Rev. Lett. **101**, 146404 (2008).
[56] J. Levrat, R. Butté, E. Feltin, J.-F. m. c. Carlin, N. Grandjean, D. Solnyshkov, and G. Malpuech, Phys. Rev. B **81**, 125305 (2010).
[57] F. Li, L. Orosz, O. Kamoun, S. Bouchoule, C. Brimont, P. Disseix, T. Guillet, X. Lafosse, M. Leroux, J. Leymarie, et al., Phys. Rev. Lett. **110**, 196406 (2013).
[58] E. Wertz, L. Ferrier, D. D. Solnyshkov, P. Senellart, D. Bajoni, A. Miard, A. Lemaître, G. Malpuech, and J. Bloch, Applied Physics Letters **95**, 051108 (2009), https://doi.org/10.1063/1.3192408.
[59] O. Jamadi, F. Réveret, D. Solnyshkov, P. Disseix, J. Leymarie, L. Mallet-Dida, C. Brimont, T. Guillet, X. Lafosse, S. Bouchoule, et al., Phys. Rev. B **99**, 085304 (2019).
[60] A. Kavokin, J. J. Baumberg, G. Malpuech, and F. P. Laussy, Microcavities (Oxford University Press, 2011).
[61] A. Gianfrate, O. Bleu, L. Dominici, V. Ardizzone, M. De Giorgi, D. Ballarini, G. Lerario, K. West, L. Pfeiffer, D. Solnyshkov, et al., Nature **578**, 381 (2020).
[62] F. Baboux, D. D. Bernardis, V. Goblot, V. N. Gladilin, C. Gomez, E. Galopin, L. L. Gratiet, A. Lemaître, I. Sagnes, I. Carusotto, et al., Optica **5**, 1163 (2018).
[63] M. Vladimirova, S. Cronenberger, D. Scalbert, K. V. Kavokin, A. Miard, A. Lemaître, J. Bloch, D. Solnyshkov, G. Malpuech, and A. V. Kavokin, Phys. Rev. B **82**, 075301 (2010).
[64] N. Takemura, S. Trebaol, M. Wouters, M. T. Portella-Oberli, and B. Deveaud, Nature Physics **10**, 500 (2014).
[65] See Supplemental Material at [xurl will be inserted by publisher], which includes Refs. [67, 73–77].
[66] M. Milićević, O. Bleu, D. D. Solnyshkov, I. Sagnes, A. Lemaître, L. L. Gratiet, A. Harouri, J. Bloch, G. Malpuech, and A. Amo, SciPost Phys. **5**, 64 (2018).
[67] I. L. Aleiner, B. L. Altshuler, and Y. G. Rubo, Phys. Rev. B **85**, 121301 (2012).
[68] D. D. Solnyshkov, A. V. Nalitov, and G. Malpuech, Physical Review Letters **116**, 046402 (2016), ISSN 0031-9007.
[69] The band edge is taken as a zero reference, because in a stationary configuration this decay is exactly compensated by the gain. All other states exhibit a stronger decay rate. The energy is measured from the band edge towards the bottom (negative mass states).
[70] M. Z. Hasan and C. L. Kane, Rev. Mod. Phys. **82**, 3045 (2010).
[71] C. Leblanc, G. Malpuech, and D. D. Solnyshkov, Phys. Rev. B **104**, 134312 (2021).
[72] T. Long, X. Ma, J. Ren, F. Li, Q. Liao, S. Schumacher, G. Malpuech, D. Solnyshkov, and H. Fu, arXiv:2110.13456 (2021).
[73] D. Tanese, H. Flayac, D. Solnyshkov, A. Amo, A. Lemaitre, E. Galopin, R. Braive, P. Senellart, I. Sagnes, G. Malpuech, et al., Nature communications **4**, 1749 (2013).
[74] M. Abbarchi, A. Amo, V. Sala, D. Solnyshkov, H. Flayac, L. Ferrier, I. Sagnes, E. Galopin, A. Lemaître, G. Malpuech, et al., Nature Physics **9**, 275 (2013).
[75] J. Kasprzak, M. Richard, A. Baas, B. Deveaud, R. André, J.-P. Poizat, and L. S. Dang, Phys. Rev. Lett. **100**, 067402 (2008), URL `https://link.aps.org/doi/10.1103/PhysRevLett.100.067402`.
[76] G. Muñoz-Matutano, A. Wood, M. Johnsson, X. Vidal, B. Q. Baragiola, A. Reinhard, A. Lemaître, J. Bloch,

A. Amo, G. Nogues, et al., Nature Materials **18**, 213 (2019).
[77] J. Nilsson, R. Stevenson, K. Chan, J. Skiba-Szymanska, M. Lucamarini, M. Ward, A. Bennett, C. Salter, I. Farrer, D. Ritchie, et al., Nature Photonics **7**, 311 (2013).